American Mineralogist, Volume 105, pages 397–408, 2020

Textural and compositional evolution of iron oxides at Mina Justa (Peru): Implications for mushketovite and formation of IOCG deposits

Xia Hu[1,2,3,4], Huayong Chen[1,5,*], Georges Beaudoin[3,4], and Yu Zhang[6]

[1]Key Laboratory of Mineralogy and Metallogeny, Guangzhou Institute of Geochemistry, Chinese Academy of Sciences, Guangzhou 510640, China
[2]University of Chinese Academy of Sciences, Beijing 100049, China
[3]Département de Géologie et de Génie Géologique, Université Laval, Québec, Québec G1V 0A6, Canada
[4]Research Center on the Geology and Engineering of Mineral Resources (E4m), Université Laval, Québec, Québec G1V 0A6, Canada
[5]Guangdong Provincial Key Laboratory of Mineral Physics and Materials, Guangzhou 510640, China
[6]School of Geosciences and info-Physics, Central South University, Changsha 410083, China

Abstract

Magnetite is a common mineral in many ore deposits and their host rocks. It contains a wide range of trace elements that can be used to fingerprint deposit types and hydrothermal processes. In this study, we present detailed textural and compositional data on magnetite of the Mina Justa deposit in southern Perú to constrain the formation of iron oxides in the iron oxide Cu-Au (IOCG) deposit type.

Two types of magnetite, i.e., mushketovite (T_{M1}) and granular (T_{M2}) magnetite, are identified based on their morphology. Mushketovite shows three different zones (central bright, dark, and outer bright) in backscattered electron (BSE) images. The central bright part (T_{M1}-1), characterized by abundant porosity and inclusions, was intensively replaced by dark magnetite of the median rim (T_{M1}-2). The outer rim (T_{M1}-3) is also bright but lacks porosity and inclusions. Granular magnetite (T_{M2}) is anhedral and shows two different brightness levels (dark and bright) in BSE images. The dark (T_{M2}-1) and bright (T_{M2}-2) domains are intergrown, with irregular boundaries. In general, the dark zones of both magnetite types (T_{M1}-2 and T_{M2}-1) are characterized by higher Si, Ca, Al, and lower Fe contents than the bright zones. Additionally, the lattice parameters of the two types of magnetite are similar and slightly lower than that of pure magnetite, indicating that some cations (e.g., Si^{4+}, Al^{3+}) whose ionic radii are smaller than Fe^{2+} or Fe^{3+} may have entered into the magnetite structure by simple or coupled substitutions.

Our study shows that oxygen fugacity and temperature change are the dominant mechanisms leading to the formation of different types of magnetite at Mina Justa. Primary hematite, identified by Raman spectroscopy, was transformed into magnetite (T_{M1}-1) due to a sharp decline of f_{O_2} and then replaced by T_{M1}-2 magnetite during temperature increase, followed by the formation of T_{M1}-3 due to decreasing temperature, eventually forming the mushketovite with different zones. The granular magnetite may have originally precipitated from hydrothermal fluid that crystallized T_{M2}-1 and also T_{M1}-2 magnetite and was then modified by changing temperature and f_{O_2} to form T_{M2}-2. Even though the iron oxides in IOCG deposits may have formed in the same alteration stage, they could undergo a very complicate evolution process. Therefore, it is important to combine texture and mineral chemistry to investigate the origin and evolution history of iron oxides.

Keywords: Iron oxides, mushketovite, texture, mineral chemistry, hydrothermal fluids, IOCG deposit

Introduction

Magnetite is a common mineral in many igneous, metamorphic, and sedimentary rocks, as well as in various Fe-containing deposit-types, including Kiruna-type, BIF (banded iron formation), magmatic Fe-Ti oxide, Fe-skarn, IOCG, and porphyry deposits (Williams et al. 2005; Liang et al. 2009; Groves et al. 2010; Sillitoe 2010; Dupuis and Beaudoin 2011; Huberty et al. 2012; Nadoll et al. 2012; Hu et al. 2015, 2017; Wen et al. 2017; Yin et al. 2017; Huang et al. 2018). Magnetite has an inverse spinel structure and typically incorporates various minor and trace elements such as Mg, Al, Ti, V, Cr, Ni, Si, Ca, and Mn into its structure (Dupuis and Beaudoin 2011; Dare et al. 2012; Nadoll et al. 2014). Previous studies have shown that compositional variety in magnetite can be used to fingerprint various deposit types or ore-forming processes (Carew 2004; Singoyi et al. 2006; Rusk et al. 2009; Dupuis and Beaudoin 2011; Dare et al. 2012; Nadoll et al. 2012; Knipping et al. 2015). However, other studies (e.g., Hu et al. 2015; Wen et al. 2017; Yin et al. 2017) have also shown that the chemical composition of magnetite can be significantly modified or reequilibrated by hydrothermal fluid.

The iron oxide-copper-gold mineralization, characterized by Cu-sulfides±Au hydrothermal mineralization with abundant magnetite and/or hematite, has been a major exploration and

* E-mail: huayongchen@gig.ac.cn

0003-004X/20/0003–397$05.00/DOI: https://doi.org/10.2138/am-2020-7024

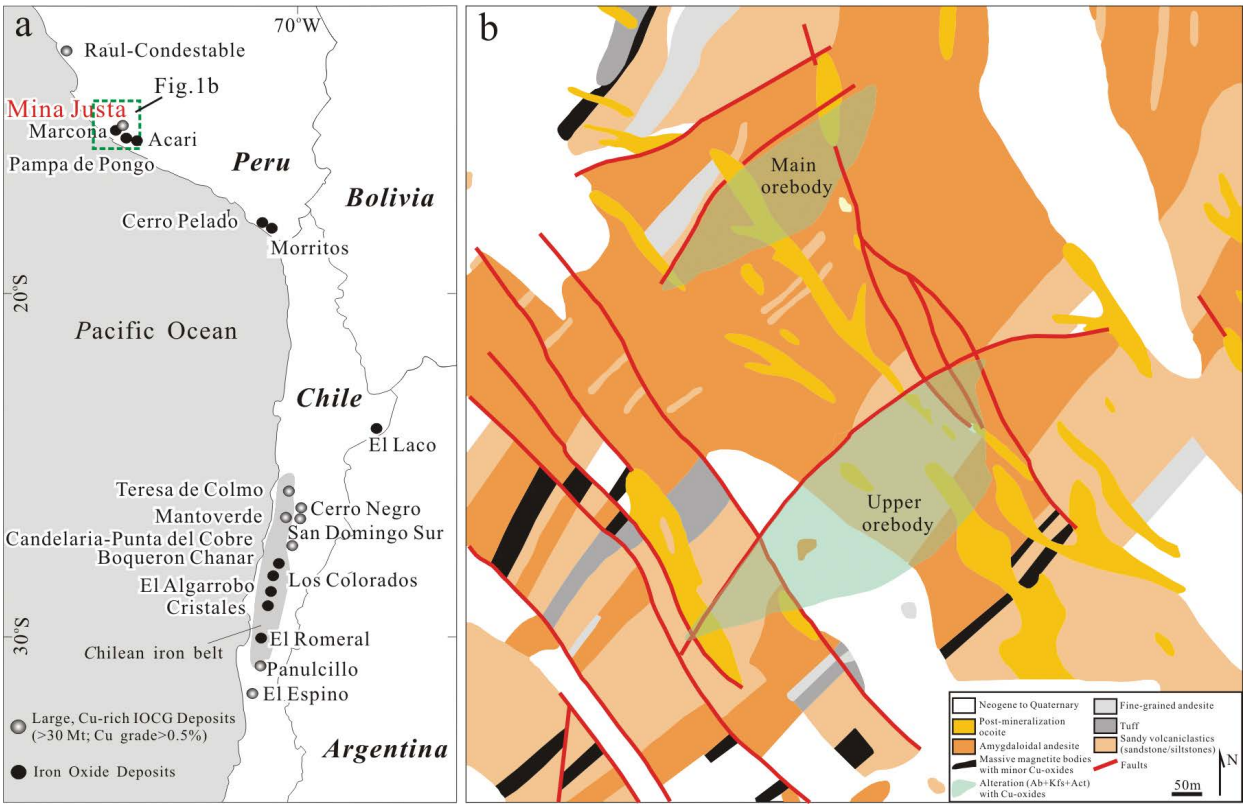

Figure 1. (**a**) The position of the Mina Justa deposit within the IOCG metallogenic belt of southern Perú. (**b**) Geological map of the Mina Justa deposit, hosted by the Middle Jurassic Upper Río Grande Formation (modified after Chen et al. 2011). Ab = albite, Act = actinolite, Kfs = K-feldspar. (Color online.)

research target since the discovery of the giant Olympic Dam Cu-U-Au (-REE) deposit (Hitzman et al. 1992). Magnetite and hematite from IOCG deposits have proven to be characterized by different trace elements, i.e., magnetite is characterized by higher Sn and Mn and lower V, Ti, Mg, Si, Cr, and Zn concentrations whereas hematite is characterized by higher As, Ga, Sb, and W concentrations (Carew 2004). Huang et al. (2018) used trace element compositions of magnetite and hematite from 16 well-studied IOCG and IOA (iron oxide apatite) deposits to investigate the links among the chemical compositions of iron oxides, hydrothermal processes, and deposit subtypes. The above studies mainly focused on presenting geochemical data of iron oxides or using trace elements in iron oxides to constrain the formation of IOCG. However, it is equally important to investigate the textural evolution of iron oxides in IOCG deposits. In addition, magnetite in IOCG deposits commonly occurs as two different forms, i.e., mushketovite (a kind of platy magnetite that is formed by replacing specular hematite.) and granular magnetite (Marschik and Fontboté 2001; Simard et al. 2006; Chen et al. 2010; Apukhtina et al. 2017). Previous studies commonly did not distinguish the two magnetite types and used their combined compositional data for deposit type discrimination (e.g., Zhibo and Chagangnuoer deposits, Günther et al. 2017). Most importantly, many researchers working on IOCG deposits usually immediately catalog "platy magnetite" as mushketovite without detailed mineralogical studies (Chen et al. 2010; Apukhtina et al. 2017). However, some studies reported that platy magnetite might be originally magnetite that was crystallized from rapid cooling of fluid (Nyström and Henríquez 1994).

In this study, we use the Mina Justa deposit as an example to investigate magnetite mineralization in IOCG deposit. We present compositional data coupled with detailed texture anatomy of two textural types of magnetite. We provide mineralogical evidence to support that platy magnetite in IOCG systems should be mushketovite. In addition, we discuss the factors controlling the magnetite chemistry and the links between the texture and chemical compositions of magnetite, to constrain the formation of iron oxides in the IOCG deposit based on these textural and geochemical analyses.

Geologic setting

The Mina Justa Cu deposit, with an indicated open pit resource of 346.6 Mt at an average grade of 0.71% Cu, 3.83 g/t Ag, and 0.03 g/t Au (Chen et al. 2011), is located in the IOCG metallogenic belt in southern Peru (Fig. 1a). The deposit is hosted by the mid-late Jurassic Upper Río Grande Formation, which is dominated by plagioclase-phyric andesite and andesitic volcaniclastic units with minor sandstone, siltstone, and limestone lenses (Fig. 1b; Caldas 1978; Hawkes et al. 2002; Baxter et al. 2005).

Two primary areas of Cu orebodies have been delimited at Mina Justa, namely the main and upper orebodies, both of which are spatially associated with nearly parallel, northeast-trending

and shallowly southeast-dipping faults, ranging from 10 to 200 m in vertical extent (Fig. 1b; Chen et al. 2010; Baxter et al. 2005). The main mineralized body crops out as a 400 m long, discontinuous belt of Cu oxides with albite-K-feldspar-actinolite alteration (Fig. 1b), which dips 10° to 30° to the southeast. The similarly northeast-trending, but northwest-dipping magnetite lenses are also exposed on surface (Fig. 1b). They commonly contain minor Cu oxides and are locally cut by the southeast-dipping Mina Justa normal faults.

Four stages of hydrothermal alteration and mineralization were recognized at Mina Justa based on the detailed petrological studies: (I) an early alteration stage; (II) the hematite stage; (III) the magnetite-pyrite stage; and (IV) the Cu mineralization stage (Fig. 2, Chen et al. 2010). Stage I alteration mainly contains albite, microcline, diopside, and actinolite. The main stages associated with iron oxides at Mina Justa are stages II and III. Therefore, we will describe these two stages in details as follows. Stage II alteration is an obliterated hematite-dominant stage inferred from the existence of "mushketovite," magnetite unambiguously pseudomorphous after specular hematite (Chen et al. 2010). The hematite may have originally formed fractured plates. Anhedral-to-subhedral, and medium- to coarse-grained calcite is intergrown with the pseudomorphs, and was replaced by quartz and magnetite (Chen et al. 2010). This stage temporally separates the early alteration and the main magnetite alteration in an andesite host. Stage III mainly contains magnetite, pyrite, quartz, and chlorite. Pyrite is medium to coarse grained and locally cut by chalcopyrite veins (Fig. 3a). Magnetite can be divided into two types based on its morphology. One is mushketovite associated with pyrite and quartz (Fig. 3a). Chalcopyrite commonly occurs interstitially in mushketovite (Fig. 3a). The second is anhedral granular magnetite that has planar grain boundaries with pyrite and quartz (Fig. 3b). The Cu mineralization stage mainly contains Cu sulfides (e.g., chalcopyrite, bornite, chalcocite).

Sampling and analytical methods

Representative samples of two types of magnetite from Stage III were selected for our study. All samples were prepared as standard polished thin sections and subsequently examined using the following analytical methods to determine the textural and compositional relationships.

Polished thin sections were carbon-coated and then investigated with a ΣIGMA scanning electron microscope (SEM) in BSE mode, at the School of Earth Science and Geological Engineering, Sun Yat-sen University (SYSU).

In situ micro-X-ray diffraction (XRD) experiments were conducted with a Rigaku D/max Rapis IIR micro-XRD system at the Central South University, Changsha, China. All measurements were carried out at 40 kV and 250 mA (Cu$K\alpha$ radiation) with a collection time of 22 min, 2θ range is 20–110°, continuous scan. The data point interval is 0.045°. The scan speed is 4°/min. The X-ray beam was ~40 μm in diameter and was focused on the selected spots on the thin sections. The software of MDI Jade 6.0 was used to analyze the obtained XRD patterns for the derivation of unit-cell parameters by whole pattern fitting. Because magnetite has a cubic structure, cell length "a" is the only parameter needed to be determined.

To identify whether hematite residue occurred in the platy magnetite, Raman spectra of magnetite were collected using a RM2000 laser micro-Raman spectrometer at the Key Laboratory of Mineralogy and Metallogeny of Guangzhou Institute of Geochemistry, Chinese Academy of Sciences (GIGCAS), Guangzhou, China. A 514.5 nm Ar laser was used, and the laser spot is 2 μm in diameter. The scanning range was between 100 and 1500 cm^{-1}. The laser power reaching the sample surface was 10 mW and the typical acquisition time was 60 s to avoid laser-induced thermal effects and oxidation.

The software of Adobe Photoshop CS4 was used to estimate the proportion of pore volume (approximately represented by area percentage) in the whole magnetite. The smallest unit of an image is a pixel, and thus the area percentage can be

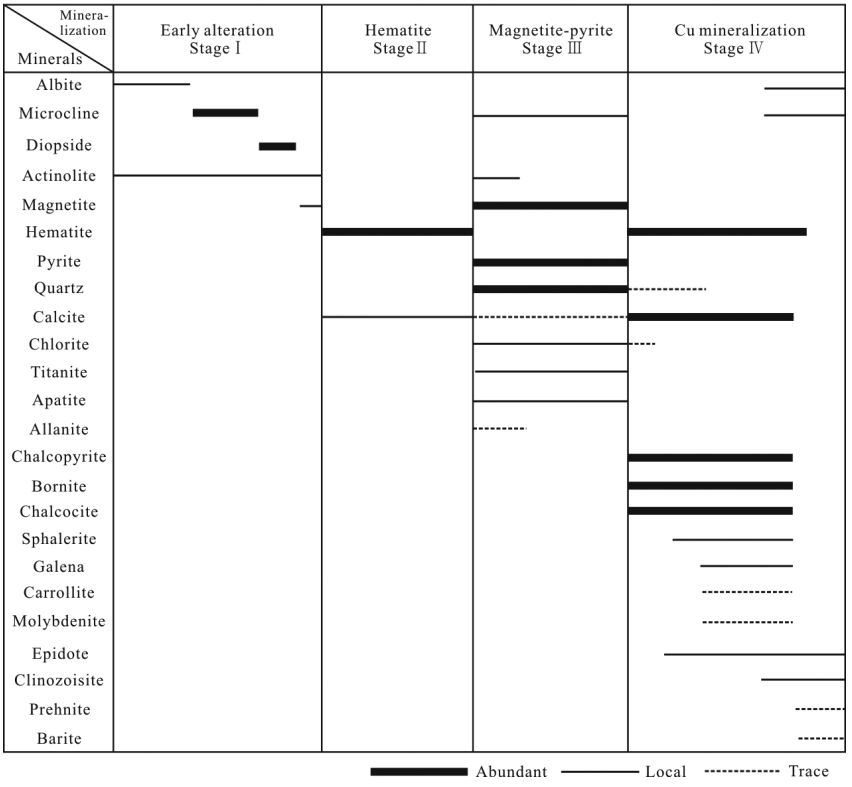

Figure 2. Alteration and mineralization paragenesis of the Mina Justa deposit. (Modified after Chen et al. 2011.)

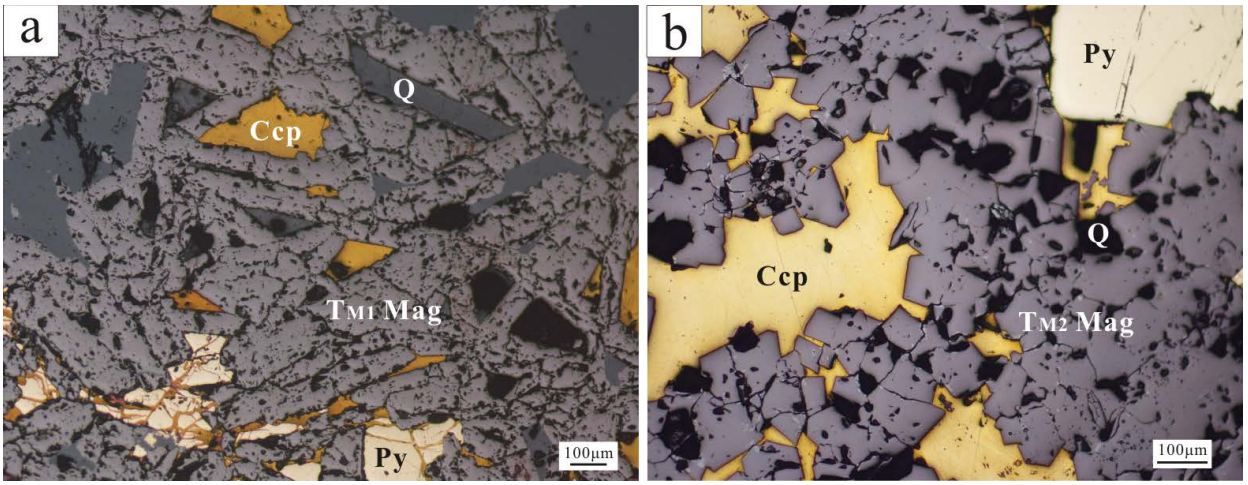

FIGURE 3. Photomicrographs of magnetite from the Mina Justa deposit. (**a**) Mushketovite intergrown with pyrite and locally cut by chalcopyrite veins. (**b**) Granular magnetite is usually anhedral and has planar grain boundaries with pyrite. Mineral abbreviations: Mag = magnetite, Ccp = chalcopyrite, Py = pyrite, Q = quartz. (Color online.)

represented by the pixel percentage. The pixels of pore area and whole magnetite area can be calculated by software, respectively. Therefore, the ratio of pixels in pore area and whole area is the proportion of pore volume in the whole magnetite.

The chemical composition of magnetite was analyzed using a JEOL JXA-8230 electron probe micro-analyzer (EPMA) at GIGCAS. The analyses were carried out with 15 kV voltage, 20 nA beam current, and 1 μm spot size. In addition, zoning in magnetite grains was mapped using EPMA for Fe, Si, Ca, and Al. The operation conditions of a voltage of 20 kV, a probe current of 300 nA, a beam size of 1 to 4 μm, and a dwell time of 100 to 200 ms for each point were used for mapping.

RESULTS

Morphology and texture of magnetite

Magnetite in the Mina Justa deposit can be classified into mushketovite (T_{M1}) and granular (T_{M2}) types. The T_{M1} magnetite commonly coexists with pyrite, quartz, and chalcopyrite (Figs. 3a and 3b). It shows three different zones (central bright, median dark, and outer bright rims) based on the SEM observation in BSE mode (Figs. 4b–4d). The central bright part (T_{M1}-1 Mag) is characterized by abundant porosity and inclusions and was replaced by the dark median rim (T_{M1}-2 Mag). Inclusions in T_{M1}-1 magnetite commonly consist of tiny W-bearing minerals such as scheelite (Fig. 4d). The outer rim (T_{M1}-3 Mag) is also bright but lacks porosity and inclusions. The T_{M2} magnetite is usually intergrown with pyrite and quartz. It is commonly anhedral and shows two different brightness in BSE images. The dark (T_{M2}-1 Mag) and bright (T_{M2}-2 Mag) domains in this magnetite are intergrown with irregular boundaries (Fig. 4f).

Structural characteristics of magnetite

XRD analysis results show that T_{M1} magnetite has a cell parameter of a = 8.3894 (0.00022) Å, which is slightly smaller than that of pure magnetite (PDF No. 19-0629, a = 8.396 Å). The cell parameter *a* of the T_{M2} magnetite is 8.3909 (0.00019) Å, which is essentially the same as that of T_{M1} magnetite within the uncertainties. The full-width at half maximum (FWHM) of the 311 peak of T_{M1} magnetite is 0.205°, and that of T_{M2} magnetite is 0.228° (Fig. 5). Hence, T_{M1} magnetite may have higher crystallinity than T_{M2} magnetite (Crepaldi et al. 2003).

All samples exhibit Raman bands characteristic of magnetite (Wang et al. 2004), including a weak peak at ~298 and two stronger ones at ~540 and ~667 cm^{-1} (Fig. 6). The central bright zone (T_{M1}-1 mag, Figs. 4c and 4d) also exhibits Raman bands indicative of hematite at ca. 225, 406, and 1320 cm^{-1} (Giarola et al. 2012; Tan et al. 2015), implying that there are still hematite residues in the T_{M1}-1 magnetite (Fig. 6).

Chemical composition of magnetite

The EMPA elemental mapping provided information on major and trace element distribution patterns within individual T_{M1} and T_{M2} magnetite crystals from the Mina Justa deposit (Fig. 7). Of the three main zones (one dark and two bright zones) in T_{M1} magnetite, the dark zone contains the highest contents of Si, Ca, Al, but the lowest Fe content (Fig. 7a). T_{M2} magnetite displays a similar variation trend as T_{M1} magnetite in which the dark domain of magnetite is characterized by higher contents of Si, Ca, Al, and lower Fe content than the bright domain (Fig. 7b).

The average, minimum, and maximum chemical contents of the Mina Justa magnetite are presented in Table 1. Mushketovite forms three compositional groups, corresponding to three different zones (Fig. 8). T_{M1}-1 magnetite has the lowest average SiO_2 (0.072 wt%), Al_2O_3 (0.047 wt%), MgO (0.016 wt%), and the highest average total FeO (92.448 wt%), whereas CaO is mostly below the detection limit (b.d.l.). T_{M1}-2 magnetite has the highest average SiO_2 (1.582 wt%), CaO (0.233 wt%), Al_2O_3 (0.324 wt%), MgO (0.12 wt%), and the lowest average total FeO (90.28 wt%). T_{M1}-3 magnetite contains moderately high average SiO_2 (0.505 wt%), CaO (0.077 wt%), Al_2O_3 (0.072 wt%), MgO (0.036 wt%), and moderately low average total FeO (91.938 wt%). These three subtypes of magnetite contain similar MnO (0.047, 0.064, 0.039 wt%, respectively), V_2O_3 (0.033, 0.033, 0.026 wt%, respectively), and TiO_2 (0.012, 0.031, 0.014 wt%, respectively) contents. The concentrations in NiO and Cr_2O_3 are mostly below the detection limit.

The granular magnetite forms two compositional groups, corresponding to two different zones (Fig. 8). T_{M2}-1 magnetite

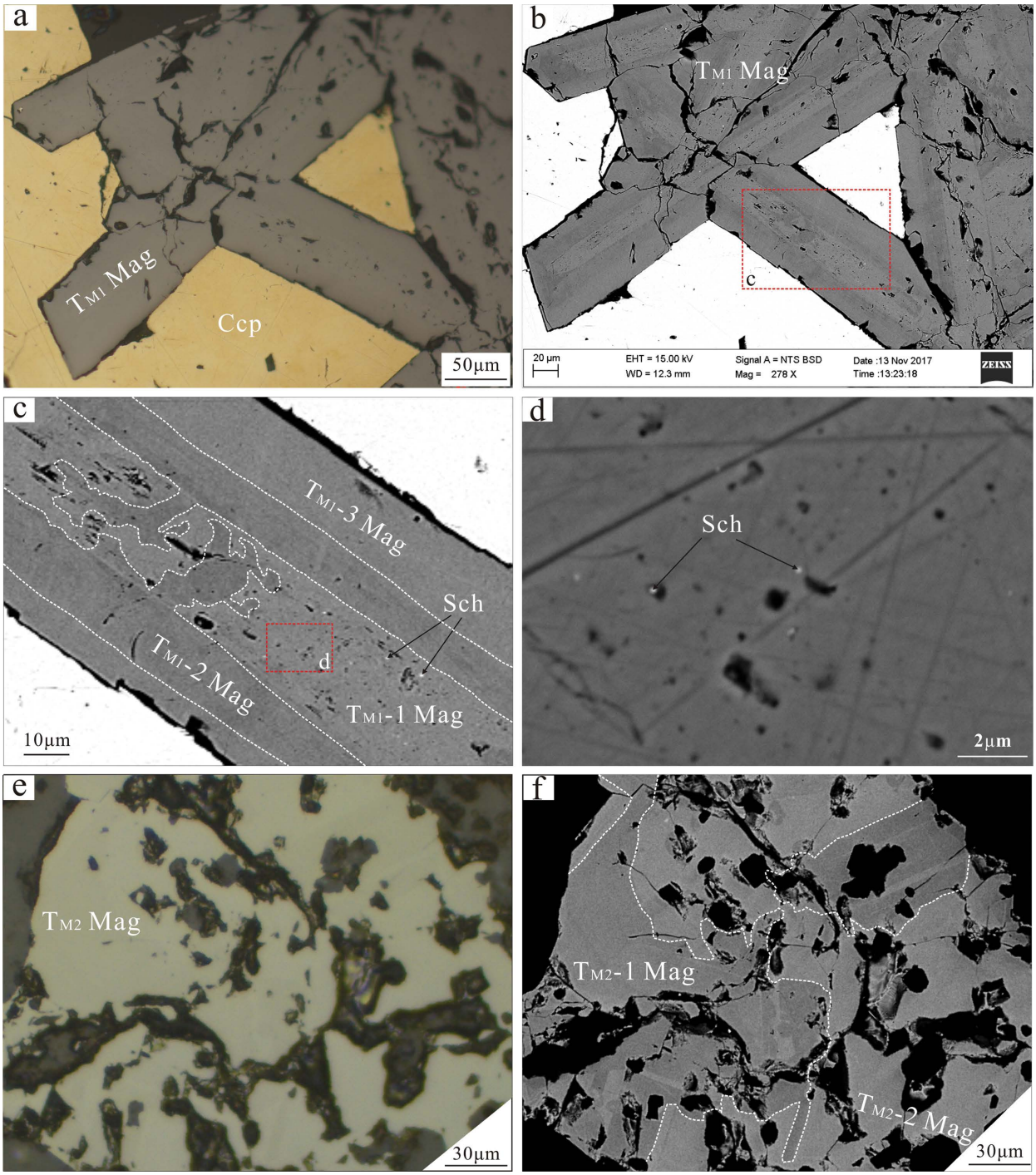

FIGURE 4. Photomicrographs (**a** and **e**) and BSE images (**b**, **c**, **d**, and **f**) of the Mina Justa magnetite. (**a**) Mushketovite (T_{M1}) with interstitial chalcopyrite. (**b**–**d**) BSE images of mushketovite, which shows different zones. T_{M1}-1 magnetite is bright with abundant porosity and inclusions. T_{M1}-2 magnetite is dark and replacing T_{M1}-1 magnetite with sharp contact between them. T_{M1}-3 magnetite is also bright but lack of porosity and inclusions. (**e**) Granular magnetite (T_{M2}). (**f**) T_{M2}-1 magnetite is replaced by T_{M2}-2 magnetite. Mineral abbreviations: Mag = magnetite, Ccp = chalcopyrite, Sch = scheelite. (Color online.)

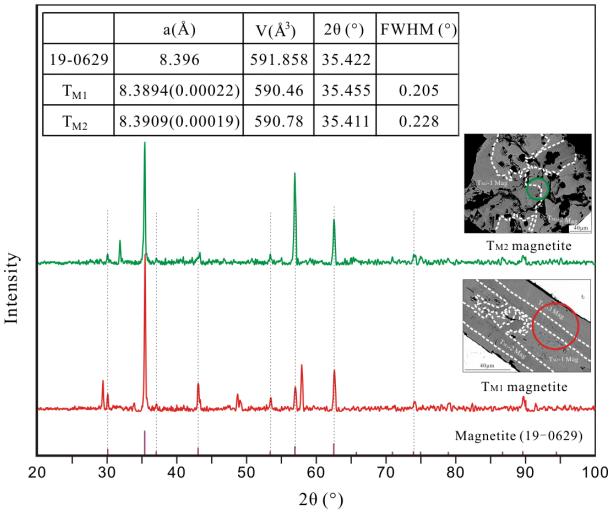

FIGURE 5. XRD patterns of magnetite from the Mina Justa deposit compared with that of a pure magnetite (19-0629). In addition to magnetite, the XRD pattern also shows the characteristic peaks of other minerals coexisting with magnetite, such as chalcopyrite (T_{M1}) and apatite (T_{M2}). The circles are 40 μm in diameter and represent the test area. (Color online.)

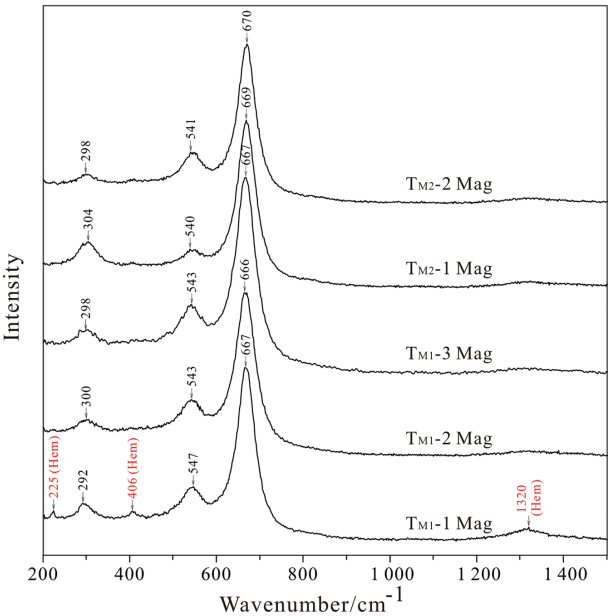

FIGURE 6. Raman spectra of different magnetite textures in the Mina Justa deposit. All samples display the characteristic peaks of magnetite, including a weak peak at ~298 cm^{-1} and two stronger at ~540 and ~667 cm^{-1}. But characteristic vibrations of hematite at ~225, ~406, and ~1320 cm^{-1} (Giarola et al. 2012) are also observed in the central bright zone of platy magnetite, which indicates that it transformed from hematite and still contains hematite residues. (Color online.)

has the higher average SiO_2 (1.365 wt%), CaO (0.247 wt%), Al_2O_3 (0.4 wt%), MgO (0.221 wt%), MnO (0.094 wt%), TiO_2 (0.146 wt%), and lower average total FeO (89.817 wt%) and V_2O_3 (0.256 wt%). T_{M2}-2 magnetite is characterized by lower average SiO_2 (0.297 wt%), Al_2O_3 (0.108 wt%), MgO (0.041 wt%), MnO (0.057 wt%), TiO_2 (0.075 wt%), and higher average total FeO (90.186 wt%), V_2O_3 (0.424 wt%). The contents of NiO, CaO, and Cr_2O_3 are mostly below the detection limit. In general, the element contents (e.g., Si, Ca, Al) of the T_{M1}-2 and T_{M1}-3 magnetite are similar to those of the T_{M2}-1 and T_{M2}-2 magnetite, respectively, whereas the concentration of V_2O_3 in T_{M1} is lower than T_{M2} magnetite (Fig. 8).

DISCUSSION

Elemental substitution mechanisms in magnetite

Magnetite has an inverse spinel structure with a general formula XY_2O_4, where X represents a divalent cation such as Fe^{2+}, Mg, Mn, Ni, Co, and Zn, and Y represents a trivalent or tetravalent cation such as Fe^{3+}, Al, V, Cr, Si, and Ti (Wechsler et al. 1984; Nadoll et al. 2014). Tetrahedral sites in the magnetite structure are exclusively occupied by the ferric (Fe^{3+}) iron atoms, whereas octahedral sites are randomly occupied by ideally equal numbers of ferric (Fe^{3+}) and ferrous (Fe^{2+}) iron atoms (Lindsley 1976; Wechsler et al. 1984; Nadoll et al. 2014). As reviewed by Nadoll et al. (2014), divalent cations such as Mg^{2+}, Mn^{2+}, Ca^{2+}, Zn^{2+}, and Ni^{2+} may enter into the magnetite structure by substituting Fe^{2+}, whereas Fe^{3+} can be replaced by some trivalent cations such as Al^{3+}, V^{3+}, and Cr^{3+}. In addition, some tetravalent cations such as Ti^{4+}, Si^{4+} may enter into the magnetite structure when coupled with the substitution of a divalent cation (Newberry et al. 1982; Wechsler et al. 1984; Westendorp et al. 1991; Xu et al. 2014).

The lattice parameter of T_{M1} magnetite (8.389 Å) is close to that of T_{M2} magnetite (8.390 Å), which are somewhat lower than that of the standard/pure magnetite (8.396 Å, Fukasawa et al. 1993). For magnetite at Mina Justa, the concentration of Fe^{3+} is negatively correlated with those of Si^{4+}, Fe^{2+}, Al^{3+} and Ca^{2+} (Figs. 9a, 9c, 9d, and 9e), whereas the Fe^{2+} content is positively correlated with Si^{4+} (Fig. 9b), which may indicate that these elements were incorporated into the structural sites of magnetite by the following substitution:

$$^{IV}Si^{4+} + {}^{VI}(Fe^{2+}, Ca^{2+}) \rightarrow {}^{IV}Fe^{3+} + {}^{VI}Fe^{3+} \quad (1)$$

$$^{IV}Al^{3+} \rightarrow {}^{IV}Fe^{3+}. \quad (2)$$

In these substitutions, both Si^{4+} and $^{IV}Al^{3+}$ have smaller ionic radii than $^{IV}Fe^{3+}$ (Shannon 1976), which may result in the lower lattice parameters of magnetite in Mina Justa compared to that of the standard magnetite. In addition, the above correlations between those ions may be resulted from the presence of small inclusions of different minerals, although they were not directly observed.

Genesis of mushketovite: Transformation of hematite to magnetite

According to the Raman spectra (Fig. 6), T_{M1}-1 magnetite (central bright zone, Fig. 4c) exhibits characteristic Raman bands of residual hematite, which indicates that the original hematite was transformed to magnetite. Such observation also provides convincing mineralogical evidence that platy magnetite should be mushketovite in previous studies at Mina Justa (Chen et al.

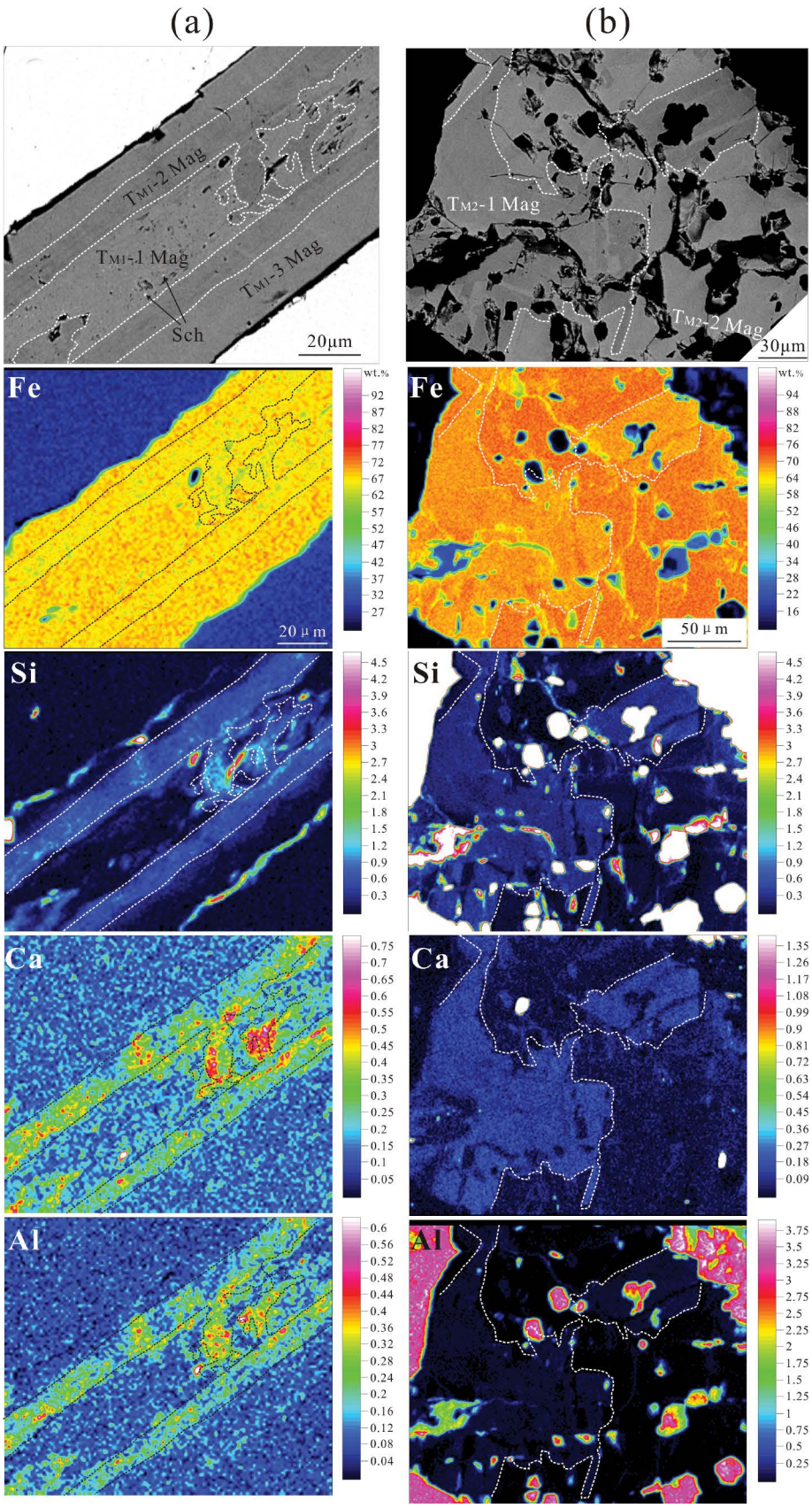

◀**FIGURE 7.** EMPA mapping of selected elements in different magnetites from the Mina Justa deposit. (**a**) Mushketovite and (**b**) granular magneite. All color scales are in weight percent. (Color online.)

TABLE 1. Mean, minimum, and maximum contents (wt%) of magnetite from the Mina Justa deposit by electron microprobe analyses

Magnetite type		SiO_2	CaO	NiO	MgO	FeO	Al_2O_3	MnO	Cr_2O_3	V_2O_3	TiO_2
T_{M1}-1 (n = 13)	Mean	0.072	b.d.l.	0.011	0.016	92.448	0.047	0.047	0.009	0.033	0.012
	Min	0.010	b.d.l.	b.d.l.	0.010	91.964	0.020	0.019	b.d.l.	b.d.l.	b.d.l.
	Max	0.294	b.d.l.	0.045	0.102	93.294	0.100	0.089	0.054	0.079	0.048
T_{M1}-2 (n = 18)	Mean	1.582	0.233	0.005	0.120	90.280	0.324	0.064	0.011	0.033	0.031
	Min	0.984	0.035	b.d.l.	0.010	88.834	0.132	0.014	b.d.l.	b.d.l.	b.d.l.
	Max	2.612	0.588	0.026	0.321	92.266	0.723	0.106	0.030	0.085	0.106
T_{M1}-3 (n = 22)	Mean	0.505	0.077	0.009	0.036	91.938	0.072	0.039	0.017	0.026	0.014
	Min	0.036	0.010	b.d.l.	0.010	90.072	0.016	b.d.l.	b.d.l.	b.d.l.	b.d.l.
	Max	0.940	0.420	0.035	0.086	94.291	0.184	0.079	0.065	0.083	0.075
T_{M2}-1 (n = 21)	Mean	1.365	0.247	0.004	0.221	89.817	0.400	0.094	0.013	0.256	0.146
	Min	1.031	0.115	b.d.l.	0.082	87.324	0.233	0.022	b.d.l.	0.046	0.075
	Max	1.898	0.383	0.045	0.437	91.236	0.690	0.155	0.060	0.561	0.237
T_{M2}-2 (n = 45)	Mean	0.297	0.011	0.008	0.041	90.186	0.108	0.057	0.015	0.424	0.075
	Min	0.013	b.d.l.	b.d.l.	0.01	88.259	0.025	0.015	b.d.l.	0.102	0.01
	Max	0.99	0.092	0.022	0.229	94.426	0.338	0.148	0.085	0.786	0.193

Note: n = numbers of analyses; b.d.l. = below detection limits.

2010) and other IOCG deposits (such as Candelaria, Chile; Marschik and Fontboté 2001).

There are two different transformation mechanisms of hematite to magnetite (Ohmoto 2003; Mucke and Cabral 2005). One is a redox reaction in which the Fe^{3+} ions in hematite are reduced to Fe^{2+} ions:

$$3Fe_2^{3+}O_3\ (Hem) + H_2 = 2Fe^{2+}Fe_2^{3+}O_4\ (Mag) + H_2O. \quad (3)$$

Another is a nonredox reaction in which the conversion of hematite to magnetite by a simple addition of Fe^{2+} ions:

$$Fe_2^{3+}O_3\ (Hem) + Fe^{2+} + H_2O = Fe^{2+}Fe_2^{3+}O_4\ (Mag) + 2H^+. \quad (4)$$

In reaction 3, the amount of Fe atoms remains constant, and there is only the removal of oxygen. According to the cell volumes of magnetite (592.704 $Å^3$; Mucke and Cabral 2005) and hematite (302.279 $Å^3$; Mucke and Cabral 2005) and the amount of Fe atoms in them (24 in magnetite and 12 in hematite), it can be calculated that the replacement of hematite by magnetite causes a volume decrease of 1.64%. In contrast, in reaction 4, the amount of Fe atoms is not constant. The reaction has an iron ratio of 2:3 between the initial and the final products, which will cause an obvious increase in volume of 47.55%. According to Ohmoto (2003), this reaction may occur in many sedimentary iron formations. For magnetite from the Mina Justa deposit, BSE images show that the central part of mushketovite (T_{M1}-1 Mag) contains abundant microporosity and inclusions (Figs. 4c and 4d). The pore volume was estimated by the software of Adobe Photoshop CS4. As shown in Figure 10a, we mark out the pore area along its contour with Polygonal Lasso Tool of Adobe Photoshop CS4, i.e., white dashed circles, and attain the pixels of pore area and whole area, respectively (Figs. 10b and 10c). As a result, the ratio of pixels in pore area and whole area is the proportion of pore volume in the whole T_{M1}-1 magnetite grain, i.e., 1.61%, which is very close to the theoretic decreased volume (1.64%) in the reaction 3. This statement suggests that the abundant micropores in T_{M1}-1 magnetite resulted from the decrease in volume during transformation of hematite to magnetite, which means the reaction 3 may have occurred under a relatively reduced environment.

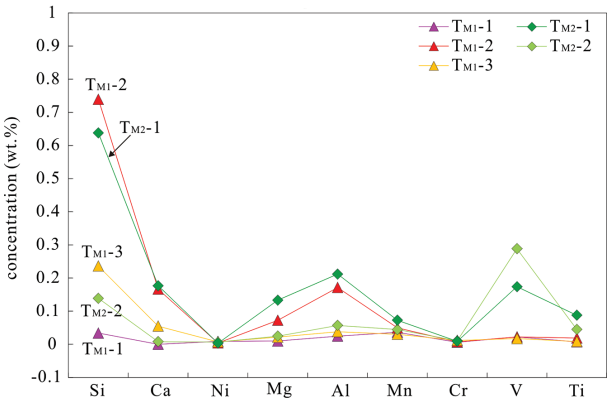

FIGURE 8. Multi-element variation diagram of the average trace element concentrations in magnetite from the Mina Justa deposit. (Color online.)

Factors controlling magnetite composition

The composition of magnetite deposited from hydrothermal fluids is controlled by several factors, such as fluid composition, nature of co-crystallizing minerals, temperature (T), and oxygen fugacity (f_{O_2}) during mineral formation (Nadoll et al. 2014). At Mina Justa, most magnetite precipitated during stage III, indicating that the two magnetite textures formed from similar hydrothermal fluids. The mushketovite and granular magnetite in Mina Justa deposit co-crystallized with the same assemblage, i.e., sulfides (pyrite and minor chalcopyrite) and quartz (with minor chlorite), suggesting the partitioning with co-crystallizing minerals had limited control on the composition of magnetite. Thus, the major controlling factors of distinct magnetite compositions at Mina Justa may be the temperature and oxygen fugacity.

Temperature is considered to be a major controlling factor for hydrothermal magnetite since element partition coefficients are temperature dependent (McIntire 1963; Sievwright et al. 2017). High-temperature porphyry and skarn magnetite show relatively high trace element contents, whereas un-metamorphosed magnetite from a banded iron formation (BIF) has the lowest trace element contents (Nadoll et al. 2014). Titanium in Fe oxides is regarded to be positively correlated with temperature (Dare et al. 2012; Nadoll et al. 2012). In addition, according to Nadoll et al. (2014), to some extent, the Ti+V vs. Al+Mn plot can reflect the variation in temperature, with high-temperature

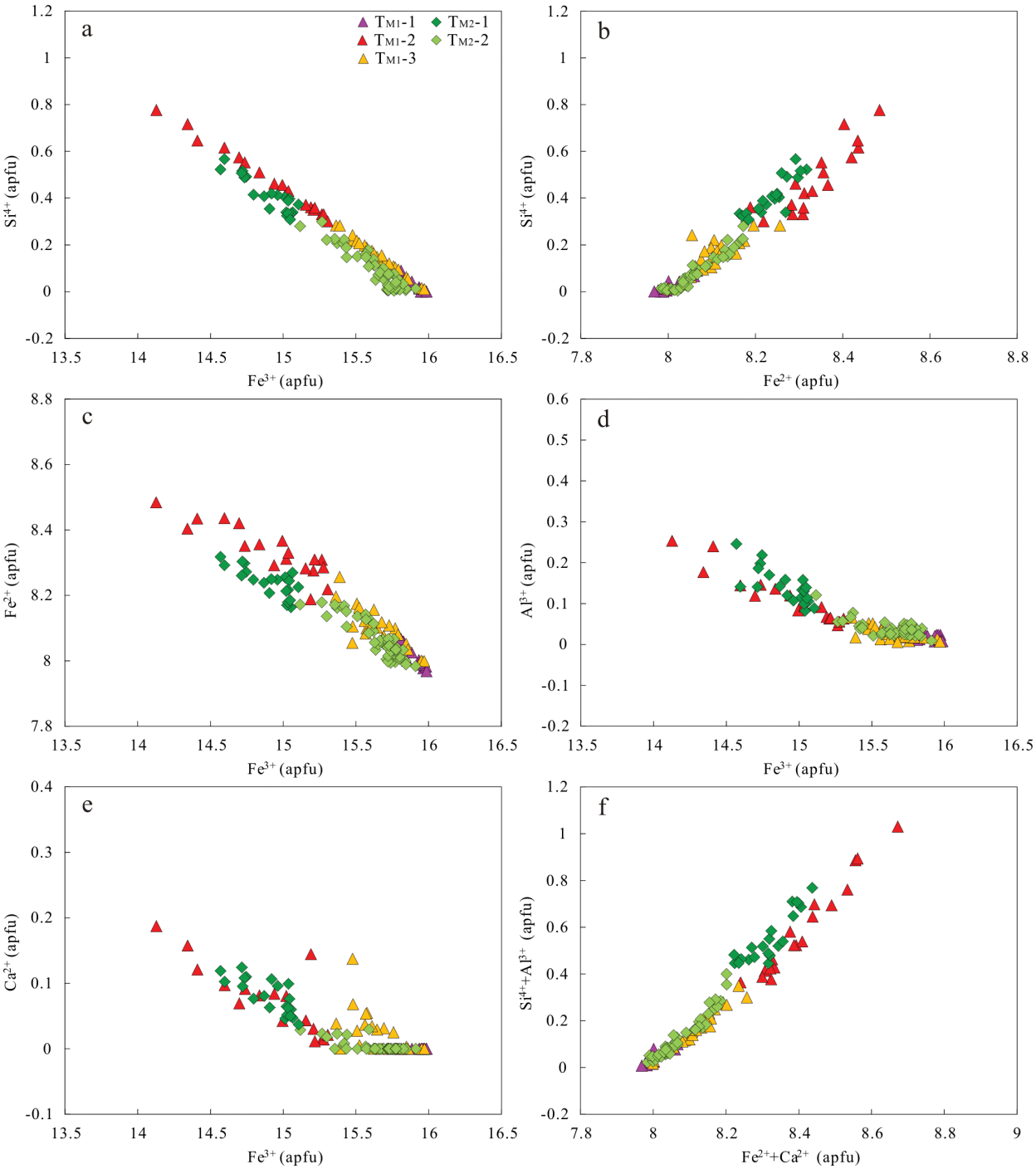

FIGURE 9. Binary plots of magnetite from the Mina Justa deposit indicating that trace elements entered into magnetite by substitution of divalent, trivalent, and/or tetravalent cations for iron. (**a**) Si^{4+} vs. Fe^{3+}; (**b**) Si^{4+} vs. Fe^{2+}; (**c**) Fe^{2+} vs. Fe^{3+}; (**d**) Al^{3+} vs. Fe^{3+}; (**e**) Ca^{2+} vs. Fe^{3+}; (**f**) $Si^{4+}+Al^{3+}$ vs. $Fe^{2+}+Ca^{2+}$. (Color online.)

magnetite plotting at high Ti+V and Al+Mn values field. T_{M1}-2 magnetite has the highest Ti+V and Al+Mn contents (Fig. 11a), indicating that temperature increased from T_{M1}-1 to T_{M1}-2, but then declined from T_{M1}-2 to T_{M1}-3 magnetite. T_{M2}-1 magnetite also has slightly higher Ti+V and Al+Mn contents than T_{M2}-2 magnetite, indicating that temperature declined from T_{M2}-1 to T_{M2}-2 magnetite. In general, T_{M2} may have formed in relatively higher temperatures than T_{M1}.

Oxygen fugacity can also impact the composition of magnetite by controlling element partition coefficients. Some

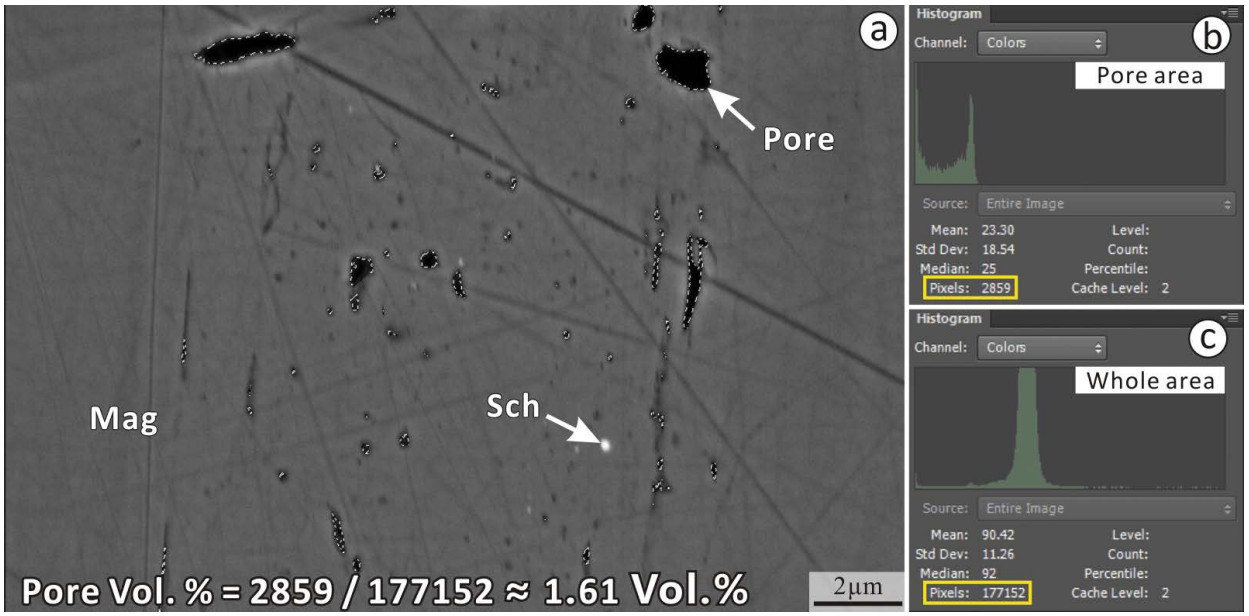

Figure 10. Estimation of pore volumes using the software Adobe Photoshop CS4. The smallest unit of an image is a pixel and thus the area percentage can be represented by the pixel percentage. (**a**) T_{M1}-1 magnetite with abundant porosity and inclusions. White dashed circles are the pores identified by the Polygonal Lasso Tool of the software. (**b**–**c**) The pixels of pore area and whole T_{M1}-1 magnetite area calculated using the software, respectively. Therefore, the ratio of pixels in pore area and whole area, i.e., 1.61%, is the proportion of pore volume in the whole T_{M1}-1 magnetite. (Color online.)

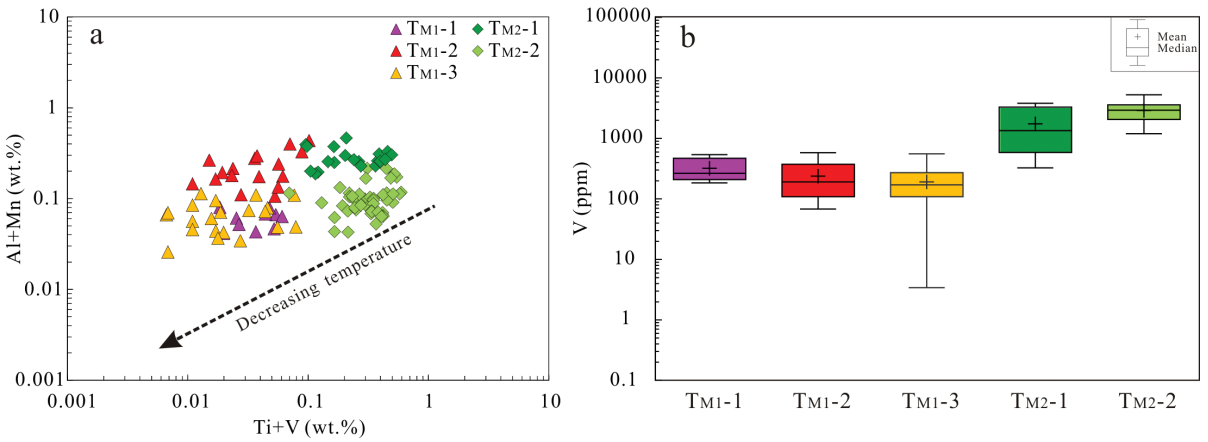

Figure 11. (**a**) Plot of (Al+Mn) vs. (Ti+V) for Mina Justa magnetite. The high-temperature magnetite usually plotted into the high Ti+V and Al+Mn values field (Nadoll et al. 2014). (**b**) Plot of V concentration for Mina Justa magnetite. V^{3+} has the highest compatibility with the spinel structure of magnetite, and V^{5+} is incompatible at high oxygen fugacity levels (Balan et al. 2006; Righter et al. 2006). Therefore, higher V concentration may indicate lower f_{O_2}. (Color online.)

elements, such as V, can occur in various valence states and therefore, their behavior is strongly linked to f_{O_2} (Nielsen et al. 1994; Righter et al. 2006). The oxidation state of V in natural environments varies from +3 to +5. Among these species, V^{3+} has the highest compatibility with the spinel structure of magnetite (Balan et al. 2006; Righter et al. 2006). Vanadium is incompatible at high oxygen fugacity levels due to its 5+ oxidation state. Therefore, the partition coefficient of magnetite/liquid for V decreases with increasing f_{O_2} because V^{3+} is less stable under these conditions. For Mina Justa magnetite, the box and whisker plot of V (Fig. 11b) shows that the V contents of T_{M1} magnetite are lower than that of T_{M2} magnetite, indicating that the f_{O_2} of T_{M1} magnetite is higher than that of T_{M2} magnetite. This is consistent with mushketovite which is formed by replacing hematite. In addition, there is no significant variation of V contents in T_{M1}-1, T_{M1}-2, and T_{M1}-3 magnetite, suggesting that there were no significant changes in f_{O_2} among different zones of mushketovite (Fig. 11b). The T_{M2}-1 magnetite has slightly lower V content, indicating that f_{O_2} slightly decreased from the T_{M2}-1 to T_{M2}-2 magnetite.

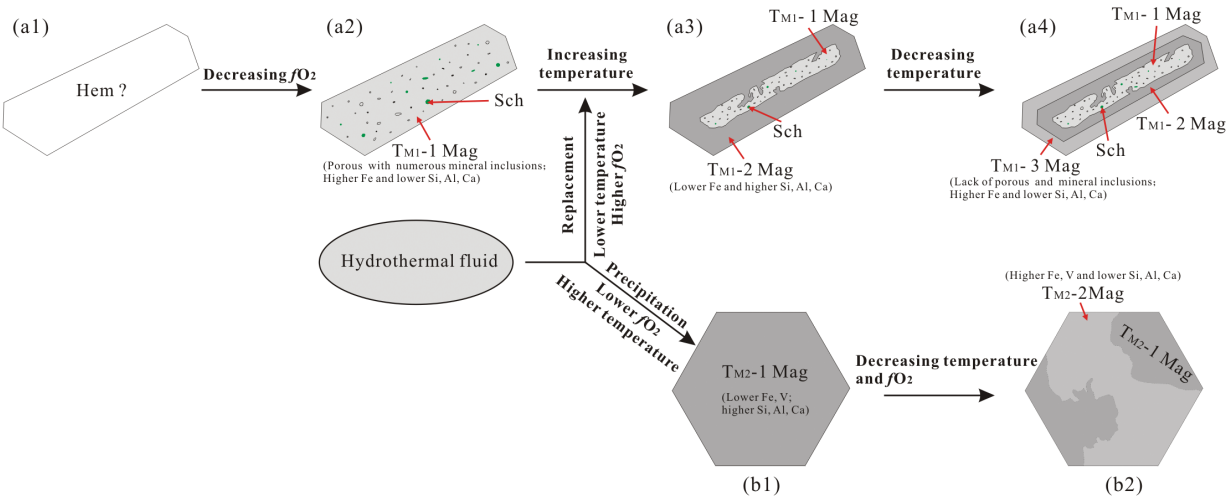

FIGURE 12. Schematic textural and chemical evolutions of iron oxides from the Mina Justa deposit. (a1–a4) primary hematite was replaced by T_{M1}-1 magnetite with a decrease of f_{O_2}. Then T_{M1}-1 magnetite was replaced by hydrothermal fluids with an increasing temperature that formed T_{M1}-2 magnetite. Finally, T_{M1}-3 magnetite was formed on the outside of T_{M1}-2 magnetite with the decrease of temperature. (b1–b2) Granular magnetite (T_{M2}-1) directly precipitated from hydrothermal fluids and then replaced by T_{M2}-2 magnetite with the decrease of temperature and f_{O_2}. (Color online.)

Evolution process of iron oxides at Mina Justa

Based on above discussion, the primary hematite (Fig. 12), which may have crystallized from an early-stage magmatic-hydrothermal fluid, was replaced by T_{M1}-1 magnetite after a sharply drop of f_{O_2} with abundant microporous and mineral inclusions due to shrinking of volume. Then T_{M1}-1 magnetite was replaced by hydrothermal fluids with increasing temperature that formed T_{M1}-2 magnetite with lower Fe and higher Si, Al, and Ca concentrations. As the temperature decreased, less Si, Al, and Ca entered into magnetite lattice to form T_{M1}-3 magnetite, which lacks micropores and mineral inclusions. Hydrothermal fluids, likely the same that formed T_{M1}-2, directly precipitated granular magnetite (T_{M2}) with sulfides and quartz, supported by the higher temperature for T_{M2} compared to T_{M1} (Figs. 11a and 12). As the temperature decreased, together with a slight decrease in f_{O_2} (Fig. 11b), T_{M2}-2 magnetite precipitated with lower Si, Al, Ca, and higher Fe and replaced T_{M2}-1 magnetite (Fig. 12).

IMPLICATIONS

This study provided mineralogical evidence to support that the platy magnetite in IOCG systems is mushketovite. In addition, textural and compositional data on magnetite from the Mina Justa deposit provide new insights into the genetic mechanism of iron oxides in IOCG deposits. Oxygen fugacity and temperature changes are the dominant mechanisms leading to the formation of different types of magnetite. The primary hematite transformed into magnetite (T_{M1}-1) due to a decline in f_{O_2} and then replaced by T_{M1}-2 magnetite with increased temperature. Meanwhile, granular T_{M2}-1 magnetite directly precipitated from hydrothermal fluid. With the decrease of temperature, T_{M1}-2 and T_{M2}-1 magnetite are replaced by T_{M1}-3 and T_{M2}-2 magnetite, respectively. This study shows that even though the iron oxides may have formed from the same alteration stage in hydrothermal deposits, they could undergo a very complicated process of evolvement.

ACKNOWLEDGMENTS

We thank Xiangping Gu (Central South University) and Changming Xing (Guangzhou Institute of Geochemistry, Chinese Academy of Sciences) for their help in the XRD and EMPA analyses. Discussion with Xiaoliang Liang and Wei Tan (Guangzhou Institute of Geochemistry, Chinese Academy of Sciences) improved the understanding of the structure of magnetite and hematite. We also acknowledge constructive comments and suggestions from Irene del Real Contreras and an anonymous reviewer, and editorial handling by M. Darby Dyar.

FUNDING

This study was funded by the National Natural Science Foundation of China (41572059 and U1603244) and the China Scholarship Council Fund (201804910485).

REFERENCES CITED

Apukhtina, O.B., Kamenetsky, V.S., Ehrig, K., Kamenetsky, M.B., Maas, R., Thompson, J., Mcphie, J., Ciobanu, C.L., and Cook, N.J. (2017) Early, deep magnetite-fluorapatite mineralization at the Olympic Dam Cu-U-Au-Ag deposit, South Australia. Economic Geology, 112, 1531–1542.

Balan, E., De Villiers, J.P.R., Eeckhout, S.G., Glatzel, P., Toplis, M.J., and Fritsch, E. (2006) The oxidation state of vanadium in titanomagnetite from layered basic intrusions. American Mineralogist, 91, 953–956.

Baxter, R., Meder, K., Cinits, R., and Berezowski, M. (2005) The Marcona copper project—Mina Justa prospect geology and mineralisation. Proceedings of the third Congreso Internacional de Prospectores y Exploradores, Lima, Conferencias, Inst de Ingenieros de Minas del Perú, Lima (CD-ROM).

Caldas, V.J. (1978) Geología de los cuadrángulos de San Juan, Acarí y Yauca: hojas, (31-m, 31-n, 32-n). Instituto de Geología y Minería, Lima, Peru.

Carew, M.J. (2004) Controls on Cu-Au mineralization and Fe oxide metasomatism in the Eastern Fold Belt, N.W. Queensland, Australia. Ph.D thesis, James Cook University, Queensland.

Chen, H.Y., Clark, A.H., Kyser, T.K., Ullrich, T.D., Baxter, R., Chen, Y.M., and Moody, T.C. (2010) Evolution of the Giant Marcona-Mina Justa Iron Oxide-Copper-Gold District, South-Central Peru. Economic Geology, 105, 155–185.

Chen, H., Kyser, T.K., and Clark, A.H. (2011) Contrasting fluids and reservoirs in the contiguous Marcona and Mina Justa iron oxide–Cu (–Ag–Au) deposits, southcentral Perú. Mineralium Deposita, 46, 677–706.

Chen, W.T., Zhou, M.F., Gao, J.F., and Hu, R. (2015) Geochemistry of magnetite from Proterozoic Fe–Cu deposits in the Kangdian metallogenic province, SW China. Mineralium Deposita, 50, 795–809.

Crepaldi, E.L., de A. A Soler-Illia, G.J., Grosso, D., and Sanchez, C. (2003) Nanocrystallised titania and zirconia mesoporous thin films exhibiting enhanced thermal stability. New Journal of Chemistry, 27, 9–13.

Dare, S.A.S., Barnes, S.-J., and Beaudoin, G. (2012) Variation in trace element content of magnetite crystallized from a fractionating sulfide liquid, Sudbury, Canada: Implications for provenance discrimination. Geochimica et Cosmo-

chimica Acta, 88, 27–50.
Dupuis, C., and Beaudoin, G. (2011) Discriminant diagrams for iron oxide trace element fingerprinting of mineral deposit types. Mineralium Deposita, 46, 319–335.
Fukasawa, T., Iwatsuki, M., and Furukawa, M. (1993) State analysis and relationship between lattice constants and compositions including minor elements of synthetic magnetite and maghemite. Analytica Chimica Acta, 281(2), 413–419.
Giarola, M., Mariotto, G., and Ajo, D. (2012) Micro-Raman investigations on inclusions of unusual habit in a commercial tanzanite gemstone. Journal of Raman Spectroscopy, 43, 556–558.
Groves, D.I., Bierlein, F.P., Meinert, L.D., and Hitzman, M.W. (2010) Iron oxide copper-gold (IOCG) deposits through Earth history: Implications for origin, lithospheric setting, and distinction from other epigenetic iron oxide deposits. Economic Geology, 105, 641–654.
Günther, T., Klemd, R., Zhang, X., Horn, I., and Weyer, S. (2017) In-situ trace element and Fe-isotope studies on magnetite of the volcanichosted Zhibo and Chagangnuoer iron ore deposits in the Western Tianshan, NW China. Chemical Geology, 453, 111–127.
Hawkes, N., Clark, A., and Moody, T. (2002) Marcona and Pampa de Pongo: giant Mesozoic Fe-(Cu, Au) deposits in the Peruvian coastal belt. Hydrothermal iron oxide copper-gold and related deposits: a global perspective. Porter Geoscience Consultancy Publishing, Adelaide, 2, 115–130.
Hitzman, M.W., Oreskes, N., and Einaudi, M.T. (1992) Geological characteristics and tectonic setting of Proterozoic iron oxide (Cu ± U ± Au ± REE) deposits. Precambrian Research, 58, 241–287.
Hu, H., Lentz, D., Li, J.-W., McCarron, T., Zhao, X.-F., and Hall, D. (2015) Reequilibration processes in magnetite from iron skarn deposits. Economic Geology, 110, 1–8.
Hu, X., Chen, H.Y., Zhao, L.D., Han, J.S., and Xia, X.P. (2017) Magnetite geochemistry of the Longqiao and Tieshan Fe-(Cu) deposits in the Middle-Lower Yangtze River Belt: Implications for deposit type and ore genesis. Ore Geology Reviews, 89, 823–835.
Huang, X.W., Boutroy, E., Makvandi, S., Beaudoin, G., and Corriveau, L. (2018) Trace element composition of iron oxides from IOCG and IOA deposits: relationship to hydrothermal alteration and deposit subtypes. Mineralium Deposita. https://doi.org/10.1007/s00126-018-0825-1.
Huberty, J.M., Konishi, H., Heck, P.R., Fournelle, J.H., Valley, J.W., and Xu, H. (2012) Silician magnetite from the Dales Gorge Member of the Brockman Iron Formation, Hamersley Group, Western Australia. American Mineralogist, 97, 26–37.
Knipping, J.L., Bilenker, L.D., Simon, A.C., Reich, M., Barra, F., Deditius, A.P., Wälle, M., Heinrich, C.A., Holtz, F., and Munizaga, R. (2015) Trace elements in magnetite from massive iron oxide-apatite deposits indicate a combined formation by igneous and magmatic-hydrothermal processes. Geochimica et Cosmochimica Acta, 171, 15–38.
Liang, H.Y., Sun, W., Su, W.C., and Zartman, R.E. (2009) Porphyry copper-gold mineralization at Yulong, China, promoted by decreasing redox potential during magnetite alteration. Economic Geology, 104, 587–596.
Lindsley, D.H. (1976) The crystal chemistry and structure of oxide minerals as exemplified by the Fe–Ti oxides. In D. Rumble III, Ed., Oxide Minerals, vol. 3, pp. L1–L60. Reviews in Mineralogy, Mineralogical Society of America, Chantilly, Virginia.
Marschik, R., and Fontboté, L. (2001) The Candelaria-Punta del Cobre iron oxide Cu-Au(-Zn-Ag) deposits, Chile. Economic Geology, 96, 1799–1826.
McIntire, W.L. (1963) Trace element partition coefficients—a review of theory and applications to geology. Geochimica et Cosmochimica Acta, 27, 1209–1264.
Mucke, A., and Cabral, A.R. (2005) Redox and nonredox reactions of magnetite and hematite in rocks.Chemie der Erde, 65, 271–278.
Nadoll, P., Mauk, J.L., Hayes, T.S., Koenig, A.E., and Box, S.E. (2012) Geochemistry of magnetite from hydrothermal ore deposits and host rocks of the Mesoproterozoic Belt Supergroup, U.S. Economic Geology, 107, 1275–1292.
Nadoll, P., Angerer, T., Mauk, J.L., French, D., and Walshe, J. (2014) The chemistry of hydrothermal magnetite: A review. Ore Geology Reviews, 61, 1–32.
Newberry, N.G., Peacor, D.R., Essene, E.J., and Geissman, J.W. (1982) Silicon in magnetite: High resolution microanalysis of magnetite-ilmenite intergrowths. Contributions to Mineralogy and Petrology, 80, 334–340.
Nielsen, R.L., Forsythe, L.M., Gallahan, W.E., and Fisk, M.R. (1994) Major- and trace-element magnetite–melt equilibria. Chemical Geology, 117, 167–191.
Nyström, J.O., and Henríquez, F. (1994), Magmatic features of iron ores of the Kiruna type in Chile and Sweden; ore textures and magnetite geochemistry. Economic Geology, 89, 820–839.
Ohmoto, H. (2003) Nonredox transformations of magnetite–hematite in hydrothermal systems. Economic Geology, 98, 157–161.
Righter, K., Leeman, W.P., and Hervig, R.L. (2006) Partitioning of Ni, Co and V between spinel-structured oxides and silicate melts: importance of spinel composition. Chemical Geology, 227, 1–25.
Rusk, B., Oliver, N., Brown, A., Lilly, R., and Jungmann, D. (2009) Barren magnetite breccias in the Cloncurry region, Australia: comparisons to IOCG deposits. In P.J. Williams, Ed., Proceedings of the 10th Biennial SGA Meeting of the Society for Geology Applied to Mineral Deposits. The Society for Geology Applied to Mineral Deposits, Townsville, Australia, p. 656–658.
Shannon, R.D. (1976) Revised effective ionic radii and systematic study of inter atomic distances in halides and chalcogenides. Acta Crystallographica, A32, 751–767.
Sievwright, R.H., Wilkinson, J.J., O'Neill, H.St.C., and Berry, A.J. (2017) Thermodynamic controls on element partitioning between titanomagnetite and andesitic-dacitic silicate melts. Contributions to Mineralogy and Petrology, 172, 62.
Sillitoe, R.H. (2010) Porphyry copper systems: Economic Geology, 105, 3–41.
Simard, M., Beaudoin, G., Bernard, J., and Hupe, A. (2006) Metallogeny of the Mont-de-l'Aigle IOCG deposit, Gaspe Peninsula, Quebec, Canada. Mineralium Deposita, 41, 607–636.
Singoyi, B., Danyushevsky, L, Davidson, G. J., Large, R., and Zaw, K. (2006) Determination of trace elements in magnetites from hydrothermal deposits using the LA-ICP-MS technique. Abstracts of Oral and Poster Presentations from the SEG 2006 Conference Society of Economic Geologist, Keystone, USA, pp. 367–368.
Tan, W., Wang, C.Y., He, H.P., Xing, C., Liang, X.L., and Dong, H. (2015) Magnetite-rutile symplectite derived from ilmenite-hematite solid solution in the Xinjie Fe-Ti oxide-bearing, mafic-ultramafic layered intrusion (SW China). American Mineralogist, 100, 2348–2351.
Wang, A., Kuebler, K.E., Jolliff, B.L., and Haskin, L.A. (2004) Raman spectroscopy of Fe-Ti-Cr-oxides, case study: Martian meteorite EETA79001. American Mineralogist, 89, 665–680.
Wechsler, B.A., Lindsley, D.H., and Prewitt, C.T. (1984) Crystal structure and cation distribution in titanomagnetites ($Fe_{3-x}Ti_xO_4$). American Mineralogist, 69, 754–770.
Wen, G., Li, J.W., Hofstra, A.H., Koenig, A.E., Lowers, H.A., and Adams, D. (2017) Hydrothermal reequilibratino of igneous magnetite in altered granitic plutons and its implications for magnetite classification schemes: Insights from the Handan-Xingtai iron district, North China Craton. Geochimica et Cosmochimica Acta, 213, 255–270.
Westendorp, R.W., Watkinson, D.H., and Jonasson, I.R. (1991) Silicon-bearing zoned magnetite crystals and the evolution of hydrothermal fluids at the Ansil Cu-Zn mine, Rouyn-Noranda, Quebec. Economic Geology, 86, 1110–1114.
Williams, P.J., Barton, M.D., Johnson, D.A., Fontbote, L., De Haller, A., Mark, G., Oliver, N.H.S., and Marschik, R. (2005) Iron oxide copper-gold deposits: Geology, space-time distribution and possible modes of origin. Economic Geology 100th Anniversary Volume, 371–405.
Xu, H., Shen, Z., and Konishi, H. (2014) Si-magnetite nano-precipitates in silician magnetite from banded iron formation: Z-contrast imaging and ab initio study. American Mineralogist, 99, 2196–2202.
Yin, S., Ma, C.Q., and Robinson, P.T. (2017) Textures and high field strength elements in hydrothermal magnetite from a skarn system: Implications for coupled dissolution-reprecipitation reactions. American Mineralogist, 102, 1045–1056.

Manuscript received February 27, 2019
Manuscript accepted November 15, 2019
Manuscript handled by M. Darby Dyar